



Research paper

Ultrafast activation efficiency of three peroxides by $\text{Fe}_{78}\text{Si}_9\text{B}_{13}$ metallic glass under photo-enhanced catalytic oxidation: A comparative study

S.X. Liang^a, Z. Jia^a, W.C. Zhang^b, X.F. Li^{a,c}, W.M. Wang^{d,*}, H.C. Lin^{e,*}, L.C. Zhang^{a,*}^a School of Engineering, Edith Cowan University, 270 Joondalup Drive, Joondalup, Perth, WA 6027, Australia^b Environmental Protection Administration of Jilin City, Jilin, Jiangxi Province 343000, China^c School of Control Technology, Wuxi Institute of Technology, Wuxi, Jiangsu Province 214121, China^d School of Materials Science and Engineering, Shandong University, Jinan, Shandong Province 250061, China^e Key Laboratory of Polar Materials and Devices, Ministry of Education, East China Normal University, Shanghai 200241, China

ARTICLE INFO

Keywords:

Catalyst
Metallic glass
Photo-enhanced
Radical generation rate
Activation

ABSTRACT

Metallic glasses with long-range disordered atomic structure have recently been attracted a great deal of research attention in catalytic field. Compared to crystalline materials, the metallic glasses present many advanced catalytic properties, yet the catalytic mechanism is not sufficiently understood. In this work, an $\text{Fe}_{78}\text{Si}_9\text{B}_{13}$ glassy ribbon manufactured by melt-spinning method was applied for the first time to compare its activation behavior on three peroxides, including hydrogen peroxide (H_2O_2), persulfate (PS) and peroxymonosulfate (PMS). It was shown that $\text{Fe}_{78}\text{Si}_9\text{B}_{13}$ metallic glass had exceptionally high capability for activating these three common peroxides to produce reactive radicals ($\cdot\text{OH}$ and/or $\text{SO}_4^{\cdot-}$). The dominant species of H_2O_2 in this work was demonstrated as hydroxyl radical ($\cdot\text{OH}$) while the PS and PMS activation mainly generated sulfate radical ($\text{SO}_4^{\cdot-}$). The order of predominant radical generation rate by $\text{Fe}_{78}\text{Si}_9\text{B}_{13}$ activation under UV-vis irradiation was PS > H_2O_2 > PMS. The relative contribution of sulfate radical ($\text{SO}_4^{\cdot-}$) in PS activation was 78% compared to 61% in PMS. All the peroxides activated by $\text{Fe}_{78}\text{Si}_9\text{B}_{13}$ metallic glass presented a radical generation rate at least ~2 times higher than other iron-containing materials. Crystal violet (CV) dye was used to investigate the catalytic performance of $\text{Fe}_{78}\text{Si}_9\text{B}_{13}$ metallic glass for peroxides, which showed an ultrafast dye degradation rate with completely color removal within 15 min. The radical evolution mechanisms for H_2O_2 , PS and PMS activation were also investigated. The change in surface morphology of ribbon after 5th run reused indicated that the inclusions of Si leading to formation of SiO_2 layer played an important role in the surface stability of ribbons.

1. Introduction

In addition to superior properties as structural materials, metallic glasses have been extensively studied to show a wide range of remarkable properties as functional materials, such as antibacterial ability in combination with plastics-like processability of Zr-based metallic glasses [1,2], superior thermal stability and good soft ferromagnetic property of Fe-based metallic glasses [3] as well as excellent biocompatibility and corrosion resistance of Ca/Ti-based metallic glasses [4,5]. In recent years, due to the advanced catalytic activity combined with other practical performances (e.g. excellent corrosion resistance property), various kinds of metallic glasses have been attracted more research attention in wastewater remediation. For example, MgZn-based amorphous powder exhibits a high degradation

capability for direct blue 6 dye and 20 times faster degradation efficiency than its crystalline counterparts [6]; Al-based glassy ribbon presents a superior applicability in wide pH conditions with the degradation efficiency in the alkaline and acidic condition having 1.5 times and 189 times, respectively, faster than in the neutral pH [7]; Co-based amorphous powder shows that the surface-area-normalized rate constant is 3 orders of magnitude higher than the commercial iron powder, leading to a ultrafast degradation rate for acid orange II solution with at least 6 times of reusability [8]. Largely owing to the low cost, friendly environmental compatibility and sustainable property with easy recycling, Fe-based metallic glasses have been emerging as the superior candidates in wastewater treatment. Different compositions of metal or metalloid have also been combined to study catalytic activity and reaction mechanism of Fe-based metallic glass. For

Abbreviations: BA, Benzoic acid; CV, Crystal violet; DSC, Differential scanning calorimetry; EDS, Energy-dispersive X-ray spectroscopy; EtOH, Ethanol; PMS, Peroxymonosulfate; PS, Persulfate; SEM, Scanning electron microscope; TBA, Tert-butanol; TEM, Transmission electron microscopy; XRD, X-ray diffraction

* Corresponding authors.

E-mail addresses: weiminw@sdu.edu.cn (W.M. Wang), hclin@ee.ecnu.edu.cn (H.C. Lin), l.zhang@ecu.edu.au, lczhangimr@gmail.com (L.C. Zhang).

instance, recent reports demonstrate that $(\text{Fe}_{0.99}\text{Mo}_{0.01})_{78}\text{Si}_9\text{B}_{13}$ glassy ribbon can almost completely decolorize direct blue 2B dye solution in 30 min at the controlled temperature of 60 °C [9]; $\text{Fe}_{73}\text{Si}_9\text{B}_{17}\text{Nb}_3$ amorphous powder is able to remove direct blue 6 with 200 times higher reactivity than Fe powder [10]; $\text{Fe}_{76}\text{B}_{12}\text{Si}_9\text{Y}_3$ amorphous powder can rapidly degrade methyl orange dye with 13 times reusability [11]. Besides, nanocrystallized Fe-based glassy ribbons (e.g. $\text{Fe}_{82.65}\text{Si}_4\text{B}_{12}\text{Cu}_{1.35}$ [12], $(\text{Fe}_{73.5}\text{Si}_{13.5}\text{B}_9\text{Nb}_3\text{Cu}_1)_{91.5}\text{Ni}_{8.5}$ [13,14]) have been reported to show an unexpectedly higher efficiency than the amorphous counterpart as the formation of galvanic cells. However, all these reactions are mostly on the basis of direct transfer of electrons [8]. Direct reduction of dye solution by glassy ribbons usually cannot obtain desirable efficiency due to relatively lower specific area compared to amorphous powders. Although a higher degradation efficiency can be achieved by ball-milled amorphous powders owing to their higher specific area and strong residual stress [10], the ball-milling procedure is needed and the manufacturing cost is thereby increased. A long processing time (up to 50 h [11]) is also required for producing ball-milled powders from ribbons. Some endeavors have been made in order to enhance the degradation performance of glassy ribbons and facilitate the operation of wastewater treatment. Recently in our previous work, the additions of 1.0 mM hydrogen peroxide (H_2O_2) and 1.0 mM persulfate (PS) were reported to highly improve complete removal of methyl blue within 15 min and 20 min, respectively, when using $\text{Fe}_{78}\text{Si}_9\text{B}_{13}$ glassy ribbons as the Fenton-like/sulfate radical-based reagent [15–20], which are based on advanced oxidation processes (AOPs).

Very recently, AOPs including ozonation [21], photocatalysis [22–24], sulfate radical-based oxidation process [25–27], Fenton/Fenton-like process [19,20] have been extensively studied as promising techniques due to their high degradation efficiency and high mineralization rate on refractory pollutants in wastewater. These oxidation processes rely on the production of reactive species with high redox potential, such as hydroxyl radicals ($\cdot\text{OH}$, $E^\circ = 2.7$ V [28]) and sulfate radicals ($\text{SO}_4^{\cdot-}$, $E^\circ = 2.5\text{--}3.1$ V [29]), to completely convert organics into H_2O , CO_2 and harmless inorganic substances [16]. The $\cdot\text{OH}$ mostly originates from hydrogen peroxide (H_2O_2) in the Fenton/Fenton-like reaction whilst the persulfate (PS) and peroxymonosulfate (PMS) are used as donors of $\text{SO}_4^{\cdot-}$ in the sulfate radical-based system. Although these three peroxides have the high self-redox potentials (1.78 V for H_2O_2 , 2.01 V for PS and 1.82 V for PMS) [30], their limited oxidation ability is still insufficient for organic compounds degradation. To improve the oxidation performance, iron salts are usually introduced to stimulate H_2O_2 to produce free radicals $\cdot\text{OH}$ in the conventional Fenton/Fenton-like process [20] while the ultraviolet (UV), heat and iron salts are favorable for $\text{SO}_4^{\cdot-}$ generation from PS or PMS in the sulfate radical-based oxidation process [25,26,30]. Apparently, iron ions play an important role in activating H_2O_2 , PS and PMS. However, adopting iron salts as Fenton reagents has several main drawbacks as follows: (1) producing additional iron sludge when pH increases [18]; (2) giving rise to secondary contamination in excessive use of iron salts [31]; (3) difficulties in reusing iron salts [32]; and (4) increased cost for disposing iron sludge in industrial scale [32]. Recently, the iron containing solid compounds in Fenton-like/sulfate radical-based process are employed as an alternative strategy to overcome some of the aforementioned disadvantages. They can be classified into (1) iron oxides (e.g. $\alpha\text{-Fe}_2\text{O}_3$ [33], $\gamma\text{-Fe}_2\text{O}_3$ [34], $\alpha\text{-FeOOH}$ [35] $\text{Fe}^0/\text{Fe}_2\text{O}_3$ [36]), (2) doped iron oxides (e.g. S/ $\alpha\text{-Fe}_2\text{O}_3$ [37], Nb/iron oxides [38], Cu-doped goethites [39]) and (3) iron oxides containing materials (e.g. magnetite [40], $\text{Bi}_2\text{WO}_6/\text{Fe}_3\text{O}_4$ [41], iron–cobalt mixed oxide [42]). Most of these iron-containing solid compounds present as powder form, which is hard to reuse (filtration and dryness are needed). The doped iron oxides and iron oxides containing materials require a series of synthesis and preparation procedures, e.g. separation of suspension from chemosynthesis before long-time dryness and calcination. On the other hand, although the iron oxides powder with the large specific

surface area have a very strong adsorption ability and they can provide much more reactive sites for peroxides reaction and pollutants decomposition, the reactive performance of some iron oxides compounds, e.g. $\alpha\text{-Fe}_2\text{O}_3$ [33], $\text{Fe}^0/\text{Fe}_2\text{O}_3$ [36], magnetite [40] iron–cobalt mixed oxide [42], in Fenton-like/sulfate radical-based reaction is somewhat bad, where more than 60 min of full removal of pollutants is needed. However, the FeSiB glassy ribbons do not require the costly surface modification and powder fabrication due to the high activation efficiency for peroxides. As the alternative Fenton reagents, Fe-based glassy ribbons have an outstanding activation efficiency for peroxides with low specific surface area and very low mass loss due to the uniquely atomic packing structure facilitating metallic glasses a lower activation energy for electron transfer, which extremely extends the active surface area and provides abundant active sites for redox reactions, thereby achieving a high catalytic reactivity [8,18]. Very recently, Fe-based glassy ribbons have demonstrated its superior reactivity in Fenton/Fenton-like and sulfate radical-based processes [15,20,43]. However, the activation behavior of Fe-based glassy ribbons on the common peroxides (H_2O_2 , PS and PMS) has rarely been discussed and compared.

In this work, a comparative study of $\text{Fe}_{78}\text{Si}_9\text{B}_{13}$ glassy ribbon on the activation for H_2O_2 , PS and PMS under photo-enhanced process is discussed. Further investigation of activation behavior of $\text{Fe}_{78}\text{Si}_9\text{B}_{13}$ glassy ribbon is based on the oxidative degradation of crystal violet (CV) dye using these three peroxides. The dominant radical evolution by $\text{Fe}_{78}\text{Si}_9\text{B}_{13}$ metallic glass is discussed and the functionality of atoms in the ribbons is also shown in detail.

2. Experimental

2.1. Materials and chemicals

The glassy ribbons with nominal composition of $\text{Fe}_{78}\text{Si}_9\text{B}_{13}$, which were cut into 5 mm wide and 20 mm long with a thickness of 30–40 μm , were manufactured by vacuum melt-spinning [44,45]. The master alloy ingot of $\text{Fe}_{78}\text{Si}_9\text{B}_{13}$ was firstly prepared by arc melting under a Ti-gettered argon atmosphere for 5 times to achieve homogenous chemical composition. From the master alloy, the glassy ribbons were fabricated by ejecting melting master alloy on a single copper roller with a wheel speed of about 30 m/s. The crystal violet (CV) dye was supplied by Wenzhou Huaqiao Chemical Reagent Co., Ltd., China. The benzoic acid (BA, $\geq 99.5\%$), oxone ($\text{KHSO}_5\text{-}0.5\text{KHSO}_4\text{-}0.5\text{K}_2\text{SO}_4$), vanadium oxide (V_2O_5 , 98%), *tert*-butanol (TBA, $\geq 99\%$) were purchased from Sigma-Aldrich. Other chemicals including sodium persulfate ($\text{Na}_2\text{S}_2\text{O}_8$), hydrogen peroxide (H_2O_2 , 30 wt.%), sodium nitrite (NaNO_2), sodium bicarbonate (NaHCO_3), potassium iodide (KI), sodium hydroxide (NaOH , 0.1 M), hydrochloric acid (HCl, 0.1 M), sulfuric acid (H_2SO_4 , 0.5 M), ethanol (EtOH, absolute) and Milli-Q water (18.2 M $\Omega\text{-cm}$) were all in the analytical grade without purification.

2.2. Characterizations

The structural features of the as-received $\text{Fe}_{78}\text{Si}_9\text{B}_{13}$ glassy ribbons were identified by X-ray diffraction (XRD) recorded on a PANalytical Empyrean diffractometer (Netherlands) with Co-K α radiation at ambient temperature and transmission electron microscopy (TEM) using a JEOL JEM-2010 microscope (Tokyo, Japan). Differential scanning calorimetry (DSC, Netzsch 404C, Germany) at a heating rate of 20 $\text{K}\cdot\text{min}^{-1}$ was used to investigate the thermal physical parameters including Curie temperature (T_c) and onset crystallization temperature (T_x) for as-received $\text{Fe}_{78}\text{Si}_9\text{B}_{13}$ glassy ribbons. The surface topography and atomic composition before and after oxidative degradation were analyzed by a scanning electron microscope (SEM, JEOL JCM-6000Plus, USA) equipped with energy-dispersive X-ray spectroscopy (EDS) detector.

2.3. Analytical methods

All the experiments for adsorption and oxidative degradation of BA and CV were carried out in a 250 mL open glass beaker by a Vortex-Genie 2 mixer (Scientific Industries, Inc. USA) at the ambient temperature. In order to achieve equilibrium absorption, the BA solution with glassy ribbons was stirred for 20 min in the darkness. Different dosages of $\text{Fe}_{78}\text{Si}_9\text{B}_{13}$ glassy ribbons with dimensions of 5×20 mm were employed throughout this work and specific concentration of peroxide (PS, PMS or H_2O_2) was also added into BA or CV solution at the beginning of each experiment, followed by external UV-vis irradiation using a 300 W Xeon simulated solar light lamp (Perfectlight Scientific Pty Ltd., Beijing, China). At given time intervals, approximately 4 mL of aqueous samples were collected from the reacting solution with characterization by UV-vis spectrometer (Shelton, CT, USA) intermediately. The absorbance peaks (λ_{max}) of BA and CV were measured to be 228 nm and 582 nm, respectively. The concentrations of PS, PMS and H_2O_2 were determined by two modified spectroscopic methods [46,47]. In the detection of PS and PMS concentrations, 4.0 g KI and 0.2 g NaHCO_3 were firstly dissolved in 40 mL Milli-Q water as stock solution then 100 μL of reacting solution at specific time was added into 4 mL stock solution. The absorbance peak located at $\lambda_{\text{max}} = 352$ nm was measured after 10 min interval for adequate reaction. In the detection of H_2O_2 concentration, 0.2 g V_2O_5 was dissolved into 100 mL H_2SO_4 (0.5 M) for preservation. Then 1 mL of reacting solution at specific time was collected and added into 5 mL firstly prepared mixture with manual shaking, after which the wavelength of absorbance was recorded at 454 nm. The H_2SO_4 (0.5 M) and HCl (0.1 M) solutions were used to control the initial pH value as 3.0 throughout PS (or PMS) experiments and H_2O_2 experiments, respectively, measured by an Oakton pH/conductivity meter (PC 2700, Cole-Parmer, USA). The total organic carbon (TOC) measurements of CV dye were conducted by a TOC-5000 CE analyzer (Shimadzu, Japan) for the mineralization analysis. Before the measurements of TOC, the oxidation reaction was quenched by adding an excess of fresh prepared NaNO_2 aqueous solution (1.0 M). In each reused experiment, a fixed 1.0 g L^{-1} dosage of identical $\text{Fe}_{78}\text{Si}_9\text{B}_{13}$ glassy ribbons were carefully separated by a fine straight tip tweezers, following with the prewash in the Milli-Q water by the ultrasonic cleaner, then further cleaning by analytical grade alcohol.

2.4. Determination of radical generation rate

For a chemical probe having an instantaneous scavenging with radicals, the rate constant of scavenging reaction must have a minimum of $10^9 \text{ M}^{-1}\text{s}^{-1}$. It is noted that benzoic acid has a reaction rate constant of $4.2 \times 10^9 \text{ M}^{-1}\text{s}^{-1}$ with $\cdot\text{OH}$ [28]. The generation rate of $\cdot\text{OH}$ ($v_{\cdot\text{OH}}$) was investigated by the competition kinetics using probe reaction between BA (as the chemical probe) and $\cdot\text{OH}$ [48,49]. The competitive objects included H_2O and oxidation intermediates. The BA had a well-defined reaction with $\cdot\text{OH}$, following with pseudo-first-order kinetics (Eq. (1)).

$$-\frac{d_{\text{BA}}}{dt} = k_{\text{BA}}[\text{BA}] \quad (1)$$

where k_{BA} is the first order rate constant. Simultaneously, the second order kinetics for $v_{\cdot\text{OH}}$ can be expressed as Eq. (2).

$$v_{\cdot\text{OH}} = k_{\cdot\text{OH},\text{BA}}[\text{BA}] [\cdot\text{OH}] + \sum k_{\cdot\text{OH},i}[\text{S}_i] [\cdot\text{OH}] \quad (2)$$

where $[\text{BA}]$ and $[\cdot\text{OH}]$ are the concentration of benzoic acid and radical species, respectively; $k_{\cdot\text{OH},\text{BA}}$ is the second order rate constant for the reaction of $\cdot\text{OH}$ with BA and $k_{\cdot\text{OH},i}$ is the second order rate constant for the reaction of $\cdot\text{OH}$ with other scavengers (S_i). The reactions of BA with other scavengers were negligible due to a high probe concentration ($[\text{BA}]/[\text{H}_2\text{O}_2] > 1000$) used, and $\cdot\text{OH}$ was fully

captured by BA. Therefore, Eq. (2) can be rewritten as Eq. (3).

$$v_{\cdot\text{OH}} = k_{\cdot\text{OH},\text{BA}}[\text{BA}] [\cdot\text{OH}] \quad (3)$$

Then the rate constant of $\cdot\text{OH}$ generation ($k_{\cdot\text{OH}}$) was calculated by plotting $\cdot\text{OH}$ generation rate ($v_{\cdot\text{OH}}$) as a function of H_2O_2 concentration ($[\text{H}_2\text{O}_2]$) (Eq. (4)).

$$v_{\cdot\text{OH}} = k_{\cdot\text{OH}}[\text{H}_2\text{O}_2] \quad (4)$$

Similarly, the generation rate of $\text{SO}_4^{\cdot-}$ was measured by the oxidation rate of a high concentration BA ($[\text{BA}]/[\text{PS (PMS)}] > 1000$) reacting with $\text{SO}_4^{\cdot-}$ (a rate constant of $1.2 \times 10^9 \text{ M}^{-1}\text{s}^{-1}$ [50]). A correct strategy for determining the quantitation of $\text{SO}_4^{\cdot-}$ was to eliminate $\cdot\text{OH}$ contribution using a radical scavenger selective to $\cdot\text{OH}$. TBA was an appropriate radical scavenger for detecting $\text{SO}_4^{\cdot-}$ due to a 3 orders of magnitude in variation of reactivity with $\text{SO}_4^{\cdot-}$ and $\cdot\text{OH}$ ($k_{\text{SO}_4^{\cdot-},\text{TBA}} = 4.0 \times 10^5 \text{ M}^{-1}\text{s}^{-1}$, $k_{\cdot\text{OH},\text{TBA}} = 6.0 \times 10^8 \text{ M}^{-1}\text{s}^{-1}$) [51]. It was widely used as a selective $\cdot\text{OH}$ scavenger in the overall contaminant decomposition [16,52]. Likely, the reaction of BA with $\text{SO}_4^{\cdot-}$ followed the pseudo-first-order kinetics (Eq. (1)). The second order kinetics for $v_{\text{SO}_4^{\cdot-},\text{+}\cdot\text{OH}}$ was expressed as Eq. (5).

$$v_{\text{SO}_4^{\cdot-},\text{+}\cdot\text{OH}} = k_{\text{SO}_4^{\cdot-},\text{BA}}[\text{BA}] [\text{SO}_4^{\cdot-}] + k_{\cdot\text{OH},\text{BA}}[\text{BA}] [\cdot\text{OH}] + \sum k_{\text{SO}_4^{\cdot-},i}[\text{S}_i] [\text{SO}_4^{\cdot-}] + \sum k_{\cdot\text{OH},i}[\text{S}_i] [\cdot\text{OH}] \quad (5)$$

where $k_{\text{SO}_4^{\cdot-},\text{BA}}$ was the second order rate constant for the reaction of $\text{SO}_4^{\cdot-}$ with BA and $k_{\text{SO}_4^{\cdot-},i}$ was the second order rate constant for the reaction of $\text{SO}_4^{\cdot-}$ with other scavengers (S_i). By employing TBA to eliminate $\cdot\text{OH}$ and a high concentration of BA, we could obtain Eq. (6).

$$v_{\text{SO}_4^{\cdot-}} = k_{\text{SO}_4^{\cdot-},\text{BA}}[\text{BA}] [\text{SO}_4^{\cdot-}] \quad (6)$$

Then the rate constant of $\text{SO}_4^{\cdot-}$ generation ($k_{\text{SO}_4^{\cdot-}}$) was regarded as the slope of the fitting line (Eq. (7)).

$$v_{\text{SO}_4^{\cdot-}} = k_{\text{SO}_4^{\cdot-}}[\text{PS (PMS)}] \quad (7)$$

The relative contributions of $\text{SO}_4^{\cdot-}$ and $\cdot\text{OH}$ from the activation of PS or PMS were measured by the variation in the rate constant with and without adding $\cdot\text{OH}$ scavenger (Eq. (8)).

Concentration of $\text{SO}_4^{\cdot-}$ (%)

$$= \left(\frac{\text{rate constant with } \cdot\text{OH} \text{ scavenger}}{\text{rate constant without } \cdot\text{OH} \text{ scavenger}} \right) \times 100\% \quad (8)$$

3. Results and discussion

3.1. Structural characterizations

The amorphous nature of the as-received ribbons is verified by XRD in Fig. 1(a). The XRD pattern displays a broad diffraction peak at a range of $2\theta = 40\text{--}60^\circ$, revealing that the as-received glassy ribbons are mainly composed of amorphous phase [53–55]. Fig. 1(a) inset shows the dark-field (DF) TEM image of as-received $\text{Fe}_{78}\text{Si}_9\text{B}_{13}$ ribbons. A small quantity of bright particles can be observed in the DF microstructure, which are confirmed as the trace of nanocrystalline precipitates of Fe_3B phase and $\alpha\text{-Fe}$ (Si) solid solution [56]. The as-received ribbons display a comparatively homogeneous amorphous matrix, indicating the ribbons are mainly in amorphous nature. According to the DSC trace in Fig. 1(b), there is no apparent glass transition can be found from the as-received $\text{Fe}_{78}\text{Si}_9\text{B}_{13}$ ribbons (as enlarged image in the inset of Fig. 1(b)). The $T_c = 680$ K indicates the permanent magnetic nature of Fe-based metallic glass and a loss of magnetism occurs over this temperature [57]. The onset crystallization temperature (T_x) is 787 K. Two obvious exothermic peaks presented at the DSC curve are attributed to different stages of crystallization, indicating the main amorphous characteristics of $\text{Fe}_{78}\text{Si}_9\text{B}_{13}$ ribbons [58].

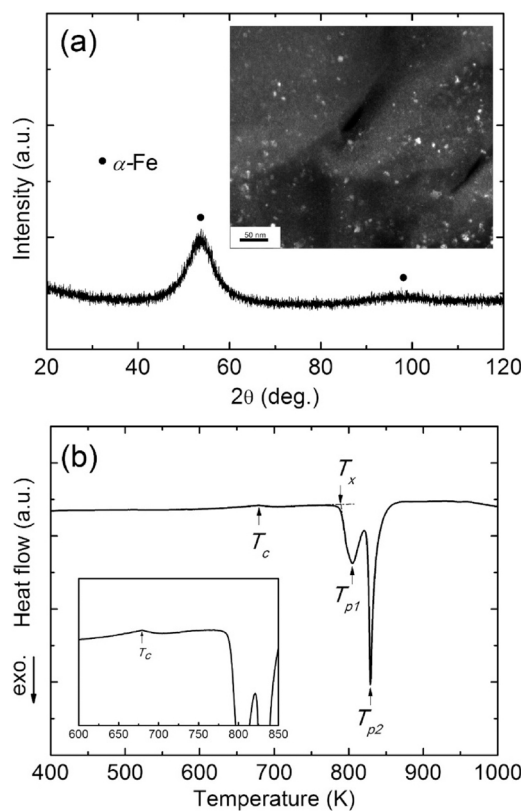


Fig. 1. (a) XRD and corresponding dark-field (DF) TEM micrograph (inset), and (b) DSC and its enlarged view (inset) of as-received $\text{Fe}_{78}\text{Si}_9\text{B}_{13}$ ribbons.

3.2. Quantitation of radicals

3.2.1. Identification of principal radical species

The chemical probe BA reacting with the radical was used for the calculation of radical generation rate, but firstly it is necessary to identify the principal radical species during peroxides activation by $\text{Fe}_{78}\text{Si}_9\text{B}_{13}$ ribbons. Fig. 2(a) shows the results of BA oxidative degradation by employing 1.0 mM to 10.0 mM of radical scavenger TBA in the activation of H_2O_2 by $\text{Fe}_{78}\text{Si}_9\text{B}_{13}$ ribbons. It is noted that $\cdot\text{OH}$ acts as the primary species in the heterogeneous Fenton reaction by Fe-based metallic glass [20]. The BA removal rate without the presence of TBA has a fast increase at the first 12 min. Then no further oxidation occurs after 16 min with a removal rate of about 32%. This result indicates that the H_2O_2 is quickly activated to produce $\cdot\text{OH}$, following with rapid consumption by BA. By increasing TBA concentration from 1.0 mM to 5.0 mM, the BA removal rate significantly decreases and there is no obvious removal of BA within 28 min when using 10.0 mM TBA. This result reveals that primary reactive species in activation of H_2O_2 is $\cdot\text{OH}$. Figs. 2(b) and (c) also present the decreasing results of BA removal rate in the activation of PS and PMS, respectively, after introducing various concentrations of TBA. As seen from Fig. 2(b), adding a low concentration of TBA from 0.2 mM to 0.5 mM has an effectively inhibitive impact on the reaction rate at the first 2 min. Further increasing of TBA concentrations to 1.0 mM and 5.0 mM results in no removal of BA within the first 2 min. However, both BA removal rates (0.2 mM and 0.5 mM TBA) increases rapidly after 2 min. According to Jia et al. [16], the PS activation by Fe-based metallic glass exhibits a two-stage activation behavior. After the pre-absorption on glassy ribbons, a dominant radical $\cdot\text{OH}$ is generated at the first 5 min followed by the conversion to $\text{SO}_4^{\cdot-}$ as the primary radical during the process of PS activation. Likely, the highly inhibition of BA removal using 0.2 mM and 0.5 mM TBA at the first 2 min indicates that the firstly generated $\cdot\text{OH}$ has been significantly scavenged, after which $\text{SO}_4^{\cdot-}$ becomes the

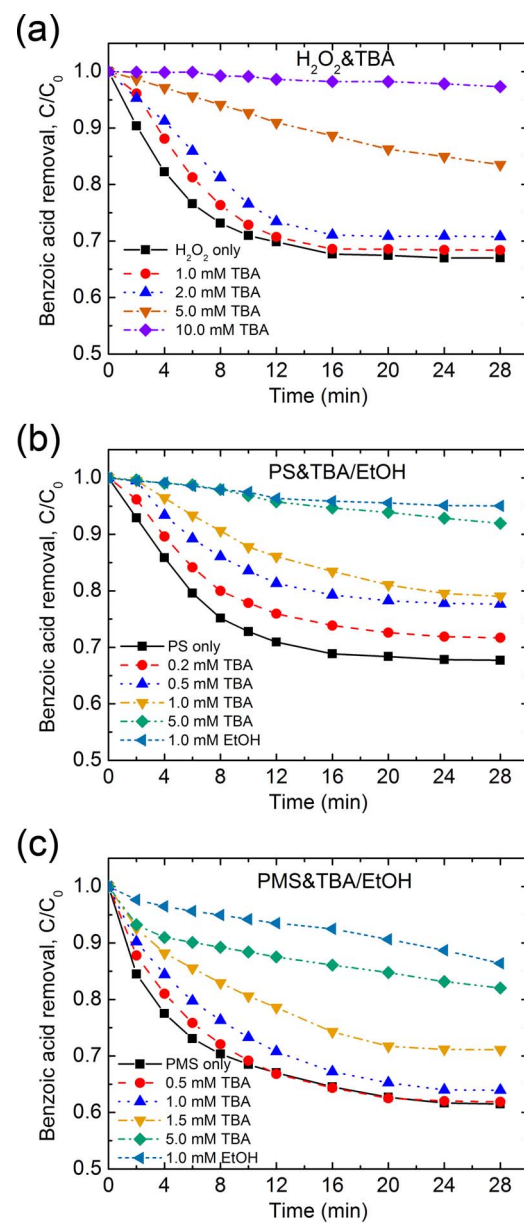


Fig. 2. Effect of radical scavengers on benzoic acid removal rate by different peroxides (a) H_2O_2 , (b) PS and (c) PMS ($\text{Fe}_{78}\text{Si}_9\text{B}_{13}$ dosage: 0.5 g L^{-1} , peroxides concentration: 0.1 mM , irradiation intensity: $14.8 \mu\text{W cm}^{-2}$, pH 3.0).

dominant radical leading to a fast degradation of BA. Notably, the predominant radical species ($\text{SO}_4^{\cdot-}$ or $\cdot\text{OH}$) in the activated PS and PMS largely depends on solution pH values [30,59]. In this work, the pH condition (3.0) may have a large contribution to the formation of $\text{SO}_4^{\cdot-}$ yielded from the activation of PS. On the other hand, the possible reason of significant decrease in BA removal rate using 5.0 mM TBA is the partially scavenging effect on $\text{SO}_4^{\cdot-}$, especially at a high concentration of TBA [60]. The reaction between TBA and $\text{SO}_4^{\cdot-}$ cannot be negligible when employing a very high concentration of TBA despite its low reaction rate with $\text{SO}_4^{\cdot-}$. In addition, there is only slight BA removal rate within 28 min when using 1.0 mM EtOH, which has scavenging effects on both $\cdot\text{OH}$ and $\text{SO}_4^{\cdot-}$ ($k_{\text{SO}_4^{\cdot-},\text{EtOH}} = 1.6 \times 10^7 \text{ M}^{-1}\text{s}^{-1}$ [29]), further confirming that the produced $\text{SO}_4^{\cdot-}$ is the dominant radical during the PS activation process. According to the aforementioned analysis, the optimal PS/TBA molar ratio is 1:5 for detecting the $\text{SO}_4^{\cdot-}$ generation rate, which will be applied in the following generation rate calculation. In terms of PMS in Fig. 2(c), the activation in PMS without scavengers at the first 2 min is

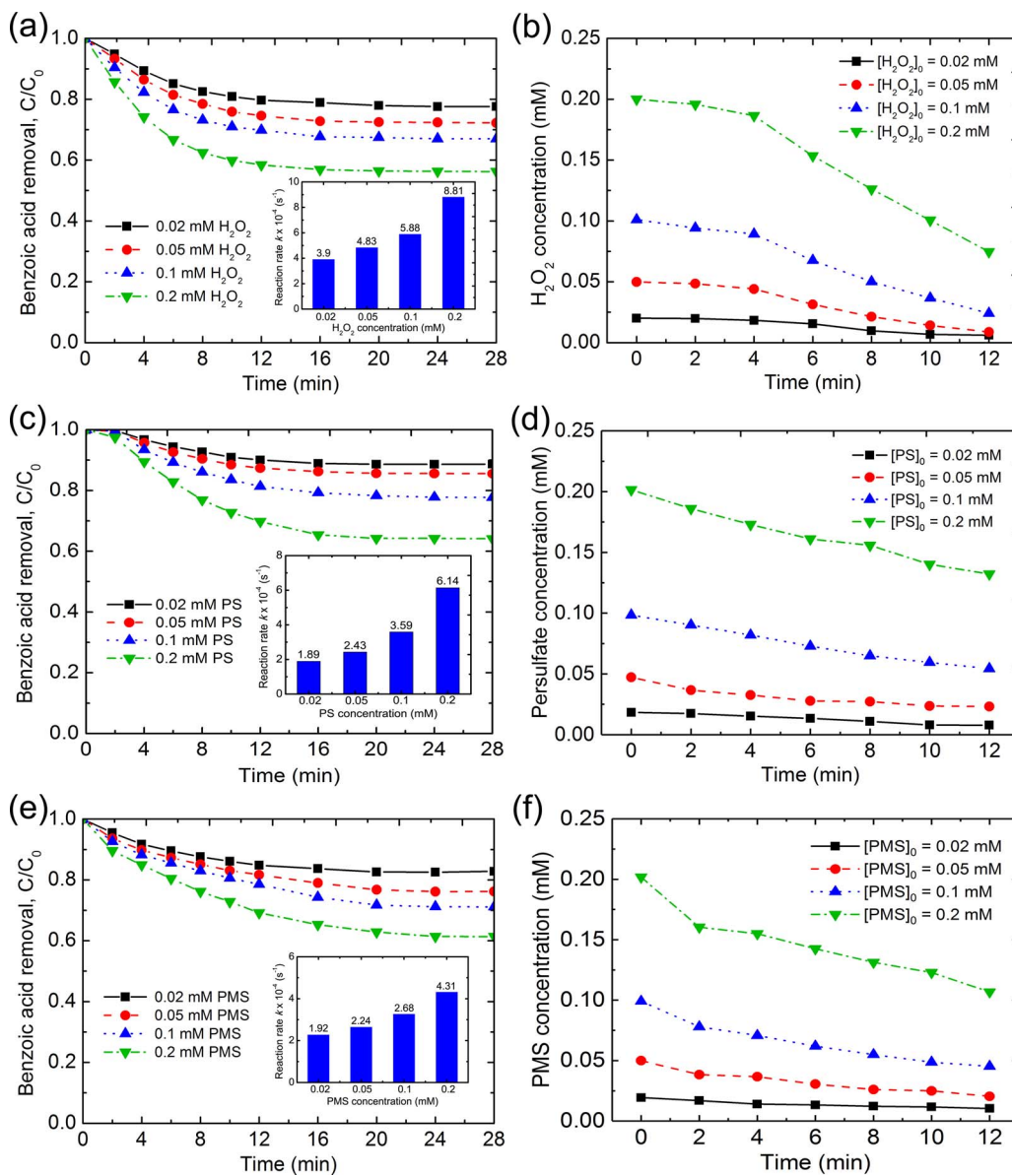


Fig. 3. (a), (c), (e) Benzocic acid removal rate over Fe₇₈Si₉B₁₃ under different initial concentration of H₂O₂, PS and PMS, respectively, (b), (d) and (f) corresponding H₂O₂, PS and PMS concentration variation along with the reaction time. (Fe₇₈Si₉B₁₃ dosage: 0.5 g L⁻¹, irradiation intensity: 14.8 μ W cm⁻², pH = 3.0).

much faster than that in PS, which results from 15.5% of BA removal rate compared to 7.1% in PS without scavengers. It can be observed that the PMS is activated easier at the first 2 min than PS under the same conditions due to the larger BA removal rate. A similar two-stage activation behavior can be observed in PMS activation. Increasing concentration of TBA up to 1.5 mM causes a dramatic reduction of BA degradation at the first 2 min. Compared to PS, the first-stage activation in PMS involves a production of \cdot OH and $\text{SO}_4^{\cdot-}$ simultaneously, leading to a removal rate remaining at around 7% at 2 min although 5.0 mM TBA is used. In addition, the usage of 1.0 mM EtOH verifies a concurrence of two active species (\cdot OH and $\text{SO}_4^{\cdot-}$) owing to the lower removal rate than using 5.0 mM TBA. Accordingly, an optimal molar ratio 1:15 of PMS to TBA concentration was used to discriminate the contributions of \cdot OH and $\text{SO}_4^{\cdot-}$ based on the results in Fig. 2(c).

3.2.2. Radicals generation rate

The BA degradation efficiency and reaction rates using Fe₇₈Si₉B₁₃ ribbons to activate three peroxides (H₂O₂, PS and PMS) are shown in Fig. 3. Various concentrations (0.02 mM, 0.05 mM, 0.1 mM and 0.2 mM) of peroxide were used. As seen from Fig. 3(a), a fast increase of BA removal rate occurs at the first 12 min for all the H₂O₂

concentrations. With increasing the H₂O₂ concentration, the BA is removed by an increasing efficiency. After the 16 min reaction of BA with \cdot OH, all of four different concentrations show a stable trend, indicating that the reactions are stabilized. The BA oxidative degradation by H₂O₂ fits well with pseudo first-order kinetics ($R^2 > 0.98$). The inset of Fig. 3(a) shows the rate constants of different H₂O₂ concentrations, increasing from 3.9×10^{-4} s⁻¹ to 8.8×10^{-4} s⁻¹ with H₂O₂ concentrations from 0.02 mM to 0.1 mM. The fast BA removal rates by H₂O₂ are also corresponding to the time-dependent concentration variations of H₂O₂ in Fig. 3(b). All the H₂O₂ with various concentrations are rapidly consumed between 4 min and 12 min, with over half of initial concentration of H₂O₂ decreasing. Such performance indicates that most H₂O₂ is activated to \cdot OH by Fe₇₈Si₉B₁₃ ribbons with assistance of UV-vis irradiation and \cdot OH further reacts with BA leading to the degradation of BA. Fig. 3(c) shows the same initial concentrations but using PS as the peroxide. The results are basically consistent with those using H₂O₂ when the PS concentration increases. However, approximate 20 min reaction time is required to achieve equilibrium and the reaction rates in PS are apparently slower than the ones using H₂O₂. One of the reasons is the addition of TBA with a molar ratio (PS:TBA = 1:5), which has the scavenging effect on \cdot OH during the

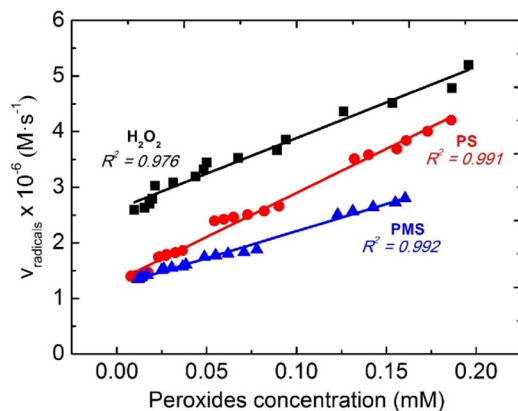


Fig. 4. Comparative radicals generation rate ($\text{Fe}_{78}\text{Si}_9\text{B}_{13}$ dosage: 0.5 g L^{-1} , irradiation intensity: $14.8 \mu\text{W cm}^{-2}$, $\text{pH} = 3.0$).

activation process of PS. The rate constants using PS concentrations of 0.02 mM , 0.05 mM , 0.1 mM and 0.2 mM are $1.89 \times 10^{-4} \text{ s}^{-1}$, $2.43 \times 10^{-4} \text{ s}^{-1}$, $3.59 \times 10^{-4} \text{ s}^{-1}$ and $6.14 \times 10^{-4} \text{ s}^{-1}$, respectively. In fact, the consumption of PS with the presence of TBA also shows a slower reduction compared with H_2O_2 (Fig. 3(d)). Fig. 3(e) presents the oxidative degradation of BA by PMS with the addition of TBA ($\text{PMS:TBA} = 1:15$). The removal rate of BA increases continuously until the reaction time at 24 min. The degradation in PMS fits well with pseudo first-order kinetics ($R^2 > 0.99$) and the PMS concentration variations at given time are showed in Fig. 3(f).

According to the calculated results from Fig. (3), the generation rate of dominant radical ($\cdot\text{OH}$ or $\text{SO}_4^{\cdot-}$) by $\text{Fe}_{78}\text{Si}_9\text{B}_{13}$ ribbons as a function of peroxides concentration is shown in Fig. 4. All the lines are regression fits of the data to Eqs. (4), (5) and (7). A summary of kinetic parameters for radical generation is shown in Table 1. Based on the generation rate constants of the dominant radical, $\text{SO}_4^{\cdot-}$ produced by activated PS has the highest efficiency. The $\text{SO}_4^{\cdot-}$ generated by PMS is the lowest one due to a relatively large amount of $\cdot\text{OH}$ produced during activation process than PS. The order of predominant radical generation rate by $\text{Fe}_{78}\text{Si}_9\text{B}_{13}$ activation under UV-vis irradiation is $\text{PS} > \text{H}_2\text{O}_2 > \text{PMS}$. According to Eq. (8), the relative contribution of $\text{SO}_4^{\cdot-}$ in PS activation can be calculated to be 78.2%, and the relative contributions of $\cdot\text{OH}$ with other scavengers are 21.8%. Likely, $\text{SO}_4^{\cdot-}$ has a relative contribution of 61% in PMS, which is lower than that of PS. This result also indicates that $\cdot\text{OH}$ plays an important role in BA removal in the PMS activation by $\text{Fe}_{78}\text{Si}_9\text{B}_{13}$ even though $\text{SO}_4^{\cdot-}$ is

responsible for the main oxidation reaction. Table 2 compares the radical generation rate constants. It is noted that radicals ($\cdot\text{OH}$ and $\text{SO}_4^{\cdot-}$) from all the three peroxides (H_2O_2 , PS and PMS) employing $\text{Fe}_{78}\text{Si}_9\text{B}_{13}$ metallic glass as Fenton-like/sulfate radical-based reagent have the extremely higher generation rate constants than other iron-containing materials (e.g. $\alpha\text{-Fe}_2\text{O}_3$, $\alpha\text{-FeOOH}$, $\text{Fe}_5\text{HO}_8\cdot 4\text{H}_2\text{O}$ and $\text{AA/Fe@Fe}_2\text{O}_3$), indicating a superior activation ability of $\text{Fe}_{78}\text{Si}_9\text{B}_{13}$ metallic glass. This superior activation behavior of metallic glass may be largely attributed to its random and uniform atomic structure leading to weak atomic bonding and far-from equilibrium state as well as an enhancement by UV-vis irradiation for the conversion from Fe^{3+} to Fe^{2+} [18].

3.3. Oxidative dye degradation

3.3.1. Effects of the experimental conditions

It is known that the dye oxidative degradation in a photo-enhanced Fenton-like or sulfate radical-based system is highly affected by the peroxide concentration, $\text{Fe}_{78}\text{Si}_9\text{B}_{13}$ dosage and irradiation intensity. As can be seen from Fig. 5(a), the peroxide concentration has a strong impact on dye degradation efficiency. The CV dye removal rate only achieves less than 20% at 30 min in the absence of peroxides. This removal rate is caused by the initial dye molecules adsorption on $\text{Fe}_{78}\text{Si}_9\text{B}_{13}$ ribbons surface and direct reductive reaction between ribbons and dye molecules [9]. Although the glassy state of $\text{Fe}_{78}\text{Si}_9\text{B}_{13}$ metallic glass facilitates reduction of CV dye, the ribbon form of metallic glasses with relatively low specific surface area inhibits its surface reactivity, leading to a long reaction time with dye. In contrast, the CV solutions are degraded in a very fast rate after employing a peroxide concentration at 1.0 mM . All the reactions present an almost complete dye removal within 15 min. According to the aforementioned discussion, it is confirmed that the primary active species ($\cdot\text{OH}$ and/or $\text{SO}_4^{\cdot-}$) with high redox potential are fast generated due to reactions between peroxides and $\text{Fe}_{78}\text{Si}_9\text{B}_{13}$ ribbons. Those radical species with large quantities ensure the dye degradation a very high efficiency.

Fig. 5(b) shows the effect of different $\text{Fe}_{78}\text{Si}_9\text{B}_{13}$ ribbon dosages on the CV dye decomposition at a constant peroxide concentration and irradiation intensity. It can be seen that using H_2O_2 alone presents a low efficiency on degrading CV dye although irradiation is applied. On the other hand, both PS and PMS alone show the similar dye removal rates of about 70% in 30 min, indicating that PS and PMS can be activated by UV-vis irradiation but in a slower reaction rate and incomplete degradation. Many researchers have investigated the performance of irradiation activations of PS and PMS as the following manners (Eqs. (9)

Table 1
Kinetic parameters for radicals generation.

		Peroxides concentration (mM)			
		0.02	0.05	0.1	0.2
H_2O_2	$k_{\text{BA}} (\text{s}^{-1})$	3.90×10^{-4}	4.83×10^{-4}	5.88×10^{-4}	8.81×10^{-4}
	$v_{\cdot\text{OH}} (\text{M} \cdot \text{s}^{-1})$	2.87×10^{-6}	3.45×10^{-6}	4.20×10^{-6}	5.71×10^{-6}
	$k_{\cdot\text{OH}} (\text{s}^{-1})$	1.28×10^{-2}			
PS	$k_{\text{BA}} (\text{s}^{-1})$	3.09×10^{-4}	3.97×10^{-4}	5.93×10^{-4}	10.3×10^{-4}
	$v_{\text{SO}_4^{\cdot-} + \cdot\text{OH}} (\text{M} \cdot \text{s}^{-1})$	2.32×10^{-6}	2.93×10^{-6}	4.15×10^{-6}	6.48×10^{-6}
	$k_{\text{SO}_4^{\cdot-} + \cdot\text{OH}} (\text{s}^{-1})$	2.02×10^{-2}			
PS + TBA	$k_{\text{BA}} (\text{s}^{-1})$	1.89×10^{-4}	2.43×10^{-4}	3.59×10^{-4}	6.14×10^{-4}
	$v_{\text{SO}_4^{\cdot-}} (\text{M} \cdot \text{s}^{-1})$	1.47×10^{-6}	1.86×10^{-6}	2.67×10^{-6}	4.27×10^{-6}
	$k_{\text{SO}_4^{\cdot-}} (\text{s}^{-1})$	1.58×10^{-2}			
PMS	$k_{\text{BA}} (\text{s}^{-1})$	2.65×10^{-4}	3.58×10^{-4}	4.98×10^{-4}	8.44×10^{-4}
	$v_{\text{SO}_4^{\cdot-} + \cdot\text{OH}} (\text{M} \cdot \text{s}^{-1})$	1.99×10^{-6}	2.59×10^{-6}	3.42×10^{-6}	5.23×10^{-6}
	$k_{\text{SO}_4^{\cdot-} + \cdot\text{OH}} (\text{s}^{-1})$	1.59×10^{-2}			
PMS + TBA	$k_{\text{BA}} (\text{s}^{-1})$	1.92×10^{-4}	2.24×10^{-4}	2.68×10^{-4}	4.31×10^{-4}
	$v_{\text{SO}_4^{\cdot-}} (\text{M} \cdot \text{s}^{-1})$	1.45×10^{-6}	1.67×10^{-6}	1.96×10^{-6}	2.99×10^{-6}
	$k_{\text{SO}_4^{\cdot-}} (\text{s}^{-1})$	0.97×10^{-2}			

Table 2Comparison of the generation rate constants of radical ($\cdot\text{OH}$ or $\text{SO}_4^{\cdot-}$) based on various Fe-based materials.

Material.	Peroxide	Probe	pH	Light ($\mu\text{W}\cdot\text{cm}^{-2}$)	$k_{\cdot\text{OH}} (\text{s}^{-1})$	$k_{\text{SO}_4^{\cdot-}} (\text{s}^{-1})$	Ref.
$\alpha\text{-Fe}_2\text{O}_3$	H_2O_2	Formic acid	4.0	–	4.0×10^{-7}	–	[49]
$\alpha\text{-FeOOH}$	H_2O_2	Formic acid	4.0	–	4.2×10^{-5}	–	[49]
$\text{Fe}_3\text{HO}_6\cdot 4\text{H}_2\text{O}$	H_2O_2	Formic acid	4.0	–	2.0×10^{-5}	–	[49]
FeOCl	H_2O_2	Benzoic acid	–	–	2.9×10^{-4}	–	[48]
$\text{AA/Fe}_2\text{O}_3$	H_2O_2	Benzoic acid	3.8	–	6.8×10^{-3}	–	[61]
$\text{Fe}_{78}\text{Si}_9\text{B}_{13}$ metallic glass	H_2O_2	Benzoic acid	3.0	14.8	1.28×10^{-2}	–	This work
$\text{Fe}_{78}\text{Si}_9\text{B}_{13}$ metallic glass	PS	Benzoic acid	3.0	14.8	–	1.58×10^{-2}	This work
$\text{Fe}_{78}\text{Si}_9\text{B}_{13}$ metallic glass	PMS	Benzoic acid	3.0	14.8	–	0.97×10^{-2}	This work

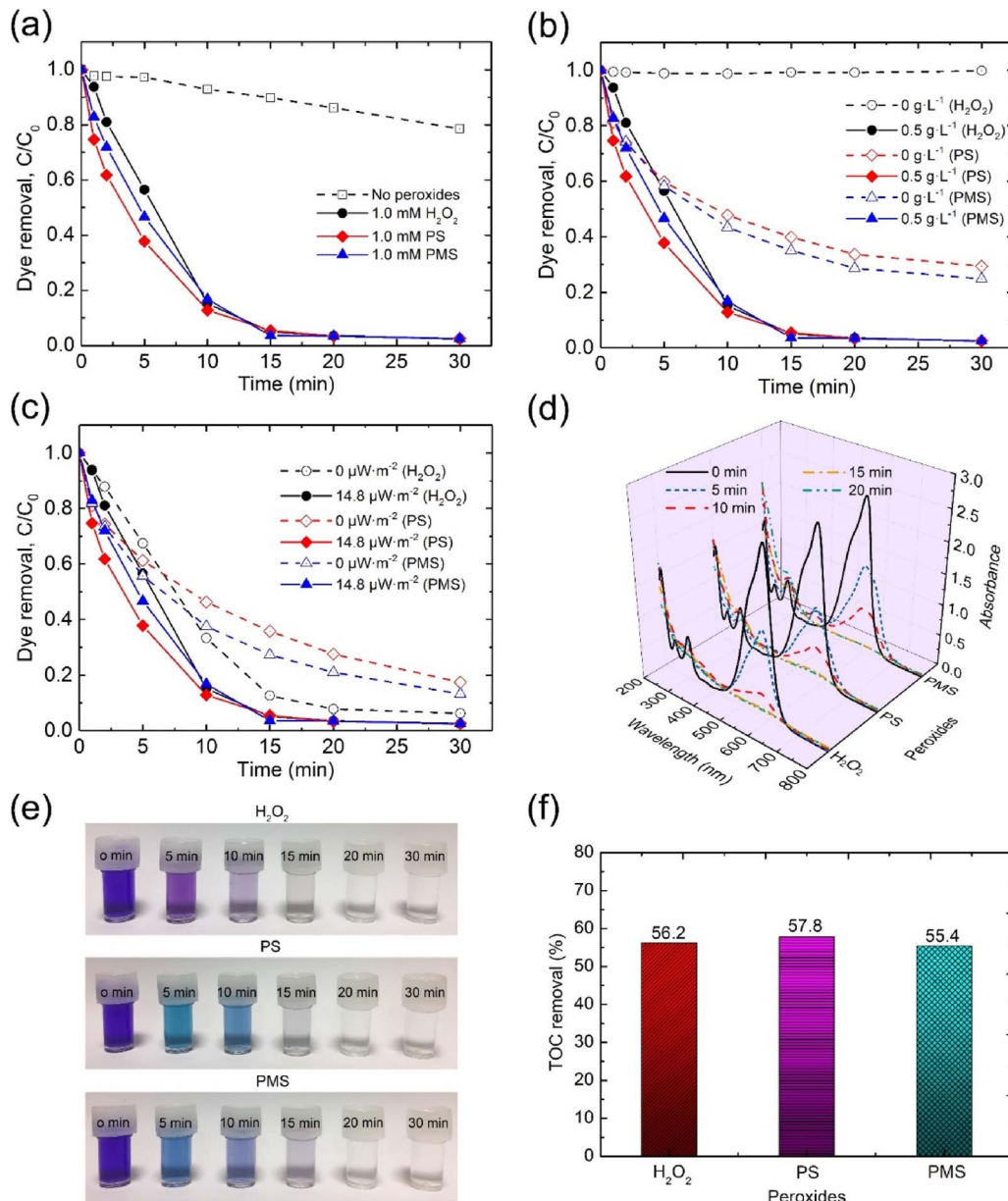
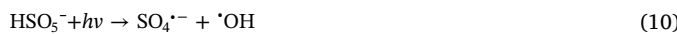


Fig. 5. Effect of (a) peroxides concentration, (b) $\text{Fe}_{78}\text{Si}_9\text{B}_{13}$ dosage, and (c) UV-vis irradiation intensity on crystal violet removal rate; (d) UV-vis spectra, (e) visible color change and (f) TOC removal rate (30 min) of crystal violet dye solution based on H_2O_2 , PS and PMS (if not mentioned, the conditions are dye concentration: 20 ppm, $\text{Fe}_{78}\text{Si}_9\text{B}_{13}$ dosage: 0.5 g L^{-1} , peroxides concentration: 1.0 mM, irradiation intensity: $14.8 \mu\text{W cm}^{-2}$, pH = 3.0). (For interpretation of the references to colour in this figure legend, the reader is referred to the web version of this article.)

and (10) [30,62]:



However, the effective degradation of contaminants by irradiation-activated PS and PMS are usually required a high concentration of peroxides and strong irradiation intensity. In this work, the activation

performances are significantly improved after the addition of 0.5 g L^{-1} glassy ribbons, especially for H_2O_2 . The CV dye removal rate of H_2O_2 improves from 10% to 100% within 15 min. Those performances strongly confirm that $\text{Fe}_{78}\text{Si}_9\text{B}_{13}$ ribbons are an excellent reagent for activating the three peroxides, which can be also verified from Fig. 5(c).

As is shown in Fig. 5(c), the effects of UV-vis irradiation intensity on dye solutions have been investigated. For the comparison, the CV

dye is degraded without applying irradiation. Those dye removal rates with $\text{Fe}_{78}\text{Si}_9\text{B}_{13}$ ribbons alone present a relative fast efficiency, indicating that $\text{Fe}_{78}\text{Si}_9\text{B}_{13}$ metallic glass can activate peroxides in a fast rate. The CV removal rates of using PS and PMS achieve about 83% and 87%, respectively, in 30 min, and of using H_2O_2 reaches about 93% in 20 min while only $\text{Fe}_{78}\text{Si}_9\text{B}_{13}$ ribbons are used. The degradation efficiency can be also enhanced after applying UV–vis irradiation, which is ascribed to easier activation of Fe electrons ($2e^-$) at $4s^2$ orbital (Eq. (11)) and sustainable generation of Fe^{2+} from Fe^{3+} under UV–vis irradiation (Eq. (12)) [18].



According to Figs. 5(a)–(c), the $\text{Fe}_{78}\text{Si}_9\text{B}_{13}$ metallic glass has the greatest impact on H_2O_2 although it can highly influence three peroxides activation efficiency while the irradiation intensity is much favorable to reactions in PS and PMS, especially PS due to a large variation of degradation efficiency before and after applying irradiation than that of PMS. In a CV degradation with the same conditions ($\text{Fe}_{78}\text{Si}_9\text{B}_{13}$ dosage: 0.5 g L^{-1} , irradiation intensity: $14.8 \mu\text{W cm}^{-2}$, pH 3.0) as chemical probe BA degradation, the CV removal rates are in a good agreement with the radical generation rate constants (k) of various peroxides in Table 1. The PS presents the highest efficiency among three peroxides, following with PMS (with both $\cdot\text{OH}$ and $\text{SO}_4^{\cdot-}$) and H_2O_2 in order. Both PS and PMS obtain a high removal rate than H_2O_2 at the first 2 min of dye removal, which is possibly caused by fast activation to produce $\cdot\text{OH}$ or/and $\text{SO}_4^{\cdot-}$, and partial decolorization ability of PS ($E^0 = 2.01 \text{ V}$) and PMS ($E^0 = 1.82 \text{ V}$) themselves. For further understanding the transformation of molecular and structural characteristics of CV dye, Fig. 5(d) shows the UV–vis spectra of photo-enhanced oxidative degradation of CV dye using H_2O_2 , PS and PMS at different time intervals. The maximum absorbance peak of CV dye located at $\lambda = 582 \text{ nm}$ indicates the conjugated chromophore structure, and peaks at $\lambda = 300 \text{ nm}$ and 247 nm originate from aromatic structures of dye molecules [63]. Noticeable, all of the main peaks at $\lambda = 582 \text{ nm}$ in these three oxidation processes become invisible along with the irradiation time, suggesting that a cleavage of chromophore ring structure occurs whilst the other two peaks in the UV region also gradually decay due to the fragmentation of the aromatic rings. The rapid decolorization of CV dye demonstrates that $\text{Fe}_{78}\text{Si}_9\text{B}_{13}$ ribbons can activate the peroxides to generate a large amount of reactive species ($\cdot\text{OH}$ and/or $\text{SO}_4^{\cdot-}$), following with *N*-demethylation (mostly by attack of active species) and oxidative degradation [64]. Such similar dye degradation pathways can be also found in processes for removal of malachite green (MG) [17]. Furthermore, the decolorization efficiency of $\text{Fe}_{78}\text{Si}_9\text{B}_{13}$ ribbons for activating H_2O_2 , PS and PMS can be verified by the progressive color change in Fig. 5(e). All the visible color of CV dye in these reactions can be removed in 15 min. Besides, the mineralization rate is also very important for analysis of oxidative degradation. As shown in Fig. 5(f), after 30 min of reaction time, all the TOC removal rates of three peroxides achieve over 55% of the initial organic carbon which has been converted into CO_2 . During the dye decomposition and mineralization, the conjugated chromophore structure is attacked by the produced reactive species leading to a fast fading of dye color while the *N*-demethylation occurs concurrently [64,65], after which the intermediates are further oxidized to harmless final inorganic products.

3.3.2. Mechanism of radical evolution on Fe-based glassy ribbon

To further verify radical species generated from peroxides activation, the quenching agents (0.5 M *tert*-butanol or/and 0.5 M ethanol) are applied in CV dye degradation. Fig. 6(a) shows a dramatic decrease of CV removal rate within 30 min after adding TBA or EtOH when H_2O_2 is used as the peroxide. The scavenging effect of TBA presents a slight stronger than EtOH, indicating that the primary active species $\cdot\text{OH}$ is

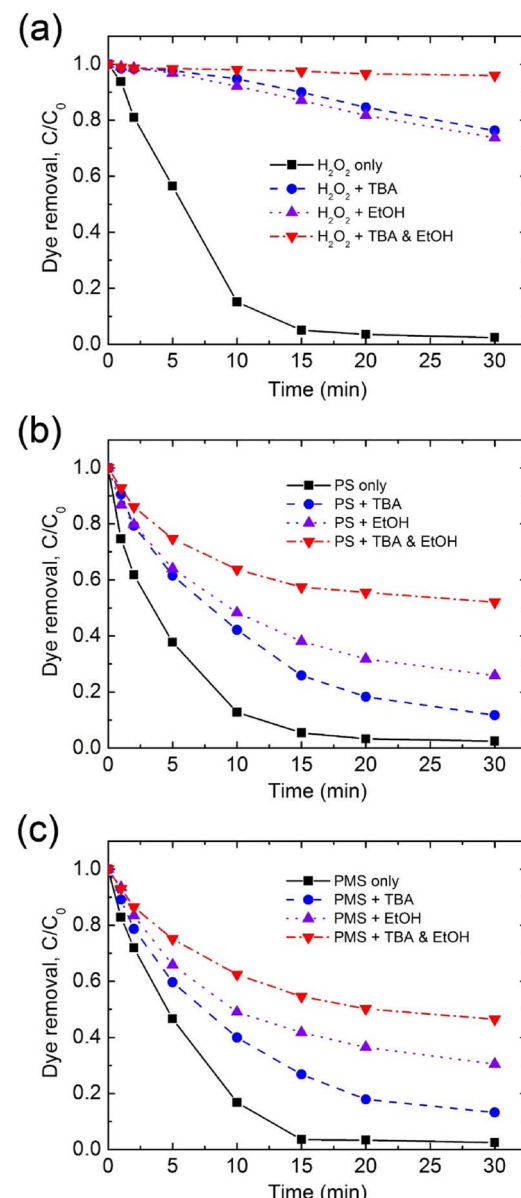
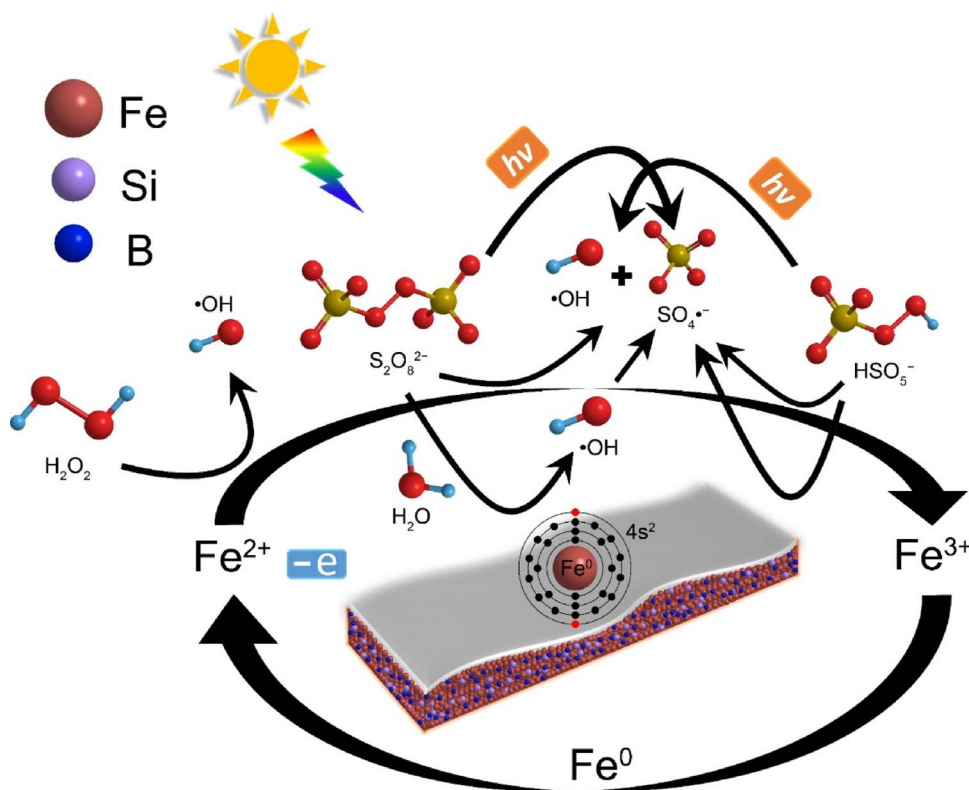


Fig. 6. Effect of *tert*-butanol (0.5 M) or/and ethanol (0.5 M) on crystal violet removal rate using various peroxides (a) H_2O_2 , (b) PS and (c) PMS (dye concentration: 20 ppm, $\text{Fe}_{78}\text{Si}_9\text{B}_{13}$ dosage: 0.5 g L^{-1} , peroxides concentration: 1.0 mM, irradiation intensity: $14.8 \mu\text{W cm}^{-2}$, pH = 3.0). (For interpretation of the references to colour in this figure legend, the reader is referred to the web version of this article.)

rapidly removed by TBA, and EtOH also has the ability to eliminate $\cdot\text{OH}$ in H_2O_2 activation process once a high concentration of scavenger ($[\text{H}_2\text{O}_2]:[\text{EtOH}] = 1:500$) is used. Obviously, there is almost no degradation of CV dye after employing both TBA and EtOH, which effectively eliminate $\cdot\text{OH}$ and highly inhibit oxidative degradation. Fig. 6(b) suggests the significant scavenging effect in the presence of TBA or/and EtOH during the PS activation. Notably, an obvious decrease in CV dye decolorization rate can be observed with the scavengers at the first 2 min compared with PS alone. The addition of EtOH has a higher scavenging effect on dye removal rate than TBA after 2 min. These performances are in agreement with the two-stage activation of PS aforementioned (Fig. 2(b)). $\cdot\text{OH}$ is firstly activated and then $\text{SO}_4^{\cdot-}$ dominates the main degradation. The dye removal by activated PMS also shows a similar inhibition behavior after the addition of TBA or/and EtOH in Fig. 6(c). However, using EtOH results in a remarkable decrease on dye removal rate at the first 2 min than TBA, suggesting that large amounts of $\text{SO}_4^{\cdot-}$ is also produced, and the active



Scheme 1. Schematic illustration for the possible radicals generation mechanisms of H_2O_2 , PS and PMS on $\text{Fe}_{78}\text{Si}_9\text{B}_{13}$ ribbon under UV-vis irradiation.

species of $\cdot\text{OH}$ and $\text{SO}_4^{\cdot-}$ coexist at the first 2 min. This is different from PS activation. After 5 min, $\text{SO}_4^{\cdot-}$ demonstrates a predominant position in PMS activation due to a higher scavenging effect using EtOH.

It is well known that Fe^{2+} acts as the main source to activate H_2O_2 , then producing active species $\cdot\text{OH}$ in the homogeneous Fenton reaction (Eq. (13)) [20]. The similar radical ($\text{SO}_4^{\cdot-}$) production manner can be also applied in homogeneous Fe^{2+} /PS and Fe^{2+} /PMS reactions (Eqs. (14) and (15), respectively) [25,26].

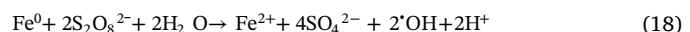


Nevertheless, in this work of H_2O_2 activation, the Fe^0 in the $\text{Fe}_{78}\text{Si}_9\text{B}_{13}$ metallic glass cannot directly reduce H_2O_2 to produce $\cdot\text{OH}$. Similar to homogeneous Fenton process, the Fe^{2+} acts as the main source of activator but the formation of Fe^{2+} in the $\text{H}_2\text{O}_2/\text{Fe}_{78}\text{Si}_9\text{B}_{13}$ system is more likely by direct reaction of solid zero-valent iron in the ribbon with a small amount of H_2O_2 molecules (Eq. (16)) [43]. In addition, the electrons of amorphous Fe atom on $4s^2$ orbital are not stable leading to extraordinarily active with external energy input [18]. An enhancement of ribbon surface corrosion thereby occurs due to application of UV-vis irradiation (Eq. (11)). The conventional Fenton reaction results in a very fast loss of Fe^{2+} whereas the $\text{Fe}^{2+}/\text{Fe}^{3+}$ cycle in the heterogeneous Fenton process is enhanced owing to reducibility of $\text{Fe}_{78}\text{Si}_9\text{B}_{13}$ (Eq. (17)). The UV-vis irradiation also accelerates the dissociation of byproduct $\text{Fe}(\text{OH})^{2+}$ into Fe^{2+} (Eq. (12)). According to the continuous generation manner above, the Fe^{2+} will react with H_2O_2 to yield appreciable amounts of $\cdot\text{OH}$.



In a PS/ $\text{Fe}_{78}\text{Si}_9\text{B}_{13}$ /UV-vis system, as suggested above, PS activation leads to a major generation of $\cdot\text{OH}$ at the first stage (2 min), which

is different from homogeneous reaction. Similar phenomenon using ZVI is also reported by Duan et al. [66]. However, a dissociation of PS only provides $\text{SO}_4^{\cdot-}$ in the reaction as Eq. (9). The generation of $\cdot\text{OH}$ is largely caused by involvement of water. It is proposed that ZVI can act as the electron donor and PS can be activated through a four-electron pathway involving water oxidation as Eq. (18) [66], of which similar activation behavior also occurs in $\text{Fe}_{78}\text{Si}_9\text{B}_{13}$ metallic glass. After the first stage activation of PS, a transition of dominant radical from $\cdot\text{OH}$ to $\text{SO}_4^{\cdot-}$ takes place along with the reaction time. The $\text{Fe}_{78}\text{Si}_9\text{B}_{13}$ ribbons follow a surface erosion by the reaction with PS for generating Fe^{2+} as H_2O_2 (Eq. (19)). Further reaction of Fe^{2+} with PS can yield adequate $\text{SO}_4^{\cdot-}$ (Eq. (14)). In addition, $\text{SO}_4^{\cdot-}$ can be formed from zero-valent iron in the ribbon without involving dissolved Fe^{2+} (Eq. (20)) [17,31], following with a small amount of $\cdot\text{OH}$ produced (Eq. (21)). Likely, a continuous generation of Fe^{2+} will happen in PS activation based on UV-vis irradiation to stimulate the loss of electrons on Fe atom, and the reducibility of $\text{Fe}_{78}\text{Si}_9\text{B}_{13}$.



In a PMS/ $\text{Fe}_{78}\text{Si}_9\text{B}_{13}$ /UV-vis system, direct surface corrosion of $\text{Fe}_{78}\text{Si}_9\text{B}_{13}$ ribbons by PMS can produce active species $\text{SO}_4^{\cdot-}$ (Eq. (22)) [67]. However, according to the results in Fig. 2(c) and Fig. 6(c), $\cdot\text{OH}$ is also detected at the first 2 min, indicating that PMS activation by UV-vis irradiation occurs simultaneously (Eq. (10)). As the significant scavenging effect of EtOH along with the reaction time, the PMS activation by $\text{Fe}_{78}\text{Si}_9\text{B}_{13}$ predominates the generation of radical species ($\text{SO}_4^{\cdot-}$), which also confirms the superior activation ability of $\text{Fe}_{78}\text{Si}_9\text{B}_{13}$ metallic glass. With the enhancement of UV-vis irradiation similar to H_2O_2 and PS, the sufficient supply of Fe^{2+} allows PMS can be quickly activated to yield appreciable amounts of $\text{SO}_4^{\cdot-}$. Notably, the PMS activation by irradiation can produce $\cdot\text{OH}$ and PMS is the main

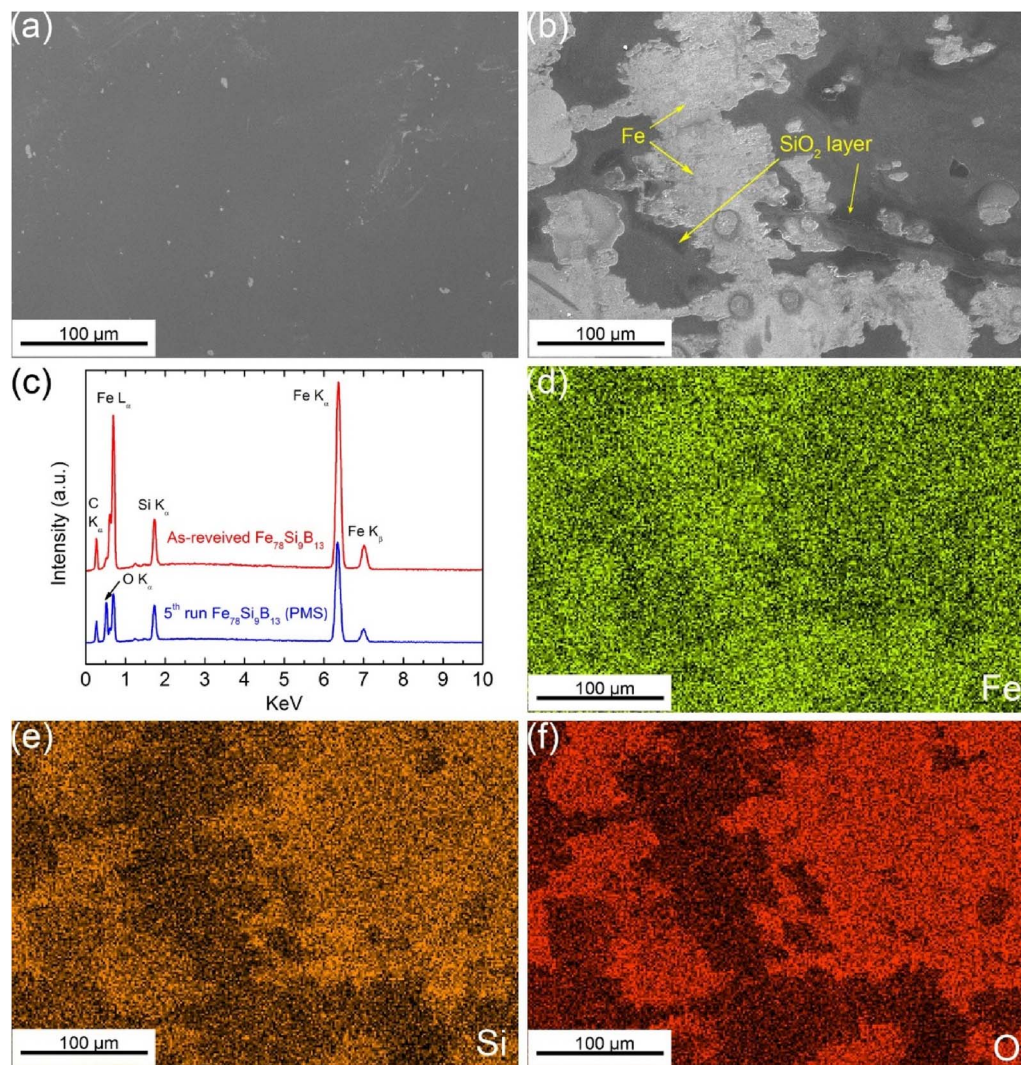


Fig. 7. SEM images of (a) as-received and (b) 5th run reused Fe₇₈Si₉B₁₃ ribbon (PMS), (c) corresponding EDS results, (d)–(f) mapping results of 5th run reused Fe₇₈Si₉B₁₃ ribbon.

donor of those active radical species, which indicate the production of ·OH is easier than PS and thereby, the total quantity of ·OH in PMS with the same condition should be larger than that in PS.



The Fe₇₈Si₉B₁₃ ribbon is not in an equilibrium state due to the amorphous structure and is energetically higher than its crystalline counterparts. In addition to the heterogeneous nature of Fe₇₈Si₉B₁₃, the surface-activated reactions more likely occur. The dye molecules (pollutants) are easily adsorbed on the ribbons surface. After the iron-activation of peroxides, those dye molecules may be oxidized by near-surface active radical species (·OH and SO₄²⁻). At the same time, the dissociative dye molecules are decomposed by free radicals in the solution. The proposed mechanisms of H₂O₂, PS and PMS activation on Fe₇₈Si₉B₁₃ glassy ribbon can be concluded in the [Scheme 1](#).

3.3.3. Surface stability

According to our previous researches for H₂O₂ and PS activation by Fe₇₈Si₉B₁₃ ribbons [\[16,18\]](#), the formation of SiO₂ layer has been demonstrated. Yet, the Fe-based metallic glass surface aging for activating PMS has not ever been reported. [Fig. 7](#) shows the SEM images and EDS results of as-received Fe₇₈Si₉B₁₃ ribbon and 5th run reused Fe₇₈Si₉B₁₃ ribbon for PMS activation. It can be observed that the surface morphology of as-received Fe₇₈Si₉B₁₃ ribbon is very smooth without obvious surface defects. After 5th run reused, the ribbon surface is overlapped by the precipitated layer, which is detected as SiO₂ layer.

[Fig. 7\(c\)](#) compares the EDS results of as-received and 5th run reused Fe₇₈Si₉B₁₃ ribbon. It is found that the intensities of Fe and Si decrease while the corresponding peak of O sharply increases, indicating the amount of Fe on the ribbon surface rapidly decreases with the surface covered by SiO₂ layer. The atom percentages of Si and O after reused suggest an increase from 10.3% to 14.0% and 1.9% to 26.7%, respectively. On the other hand, the atom percentage of Fe decreases from 87.8% to 59.3%. Further verifying elemental composition of the oxide film on the ribbon after 5th run reused is shown in [Figs. 7\(d\)–\(f\)](#). The Fe mapping result shows a highlighted region which is coincident with the Fe region in [Fig. 7\(b\)](#), suggesting a high concentration of Fe exposed on the ribbon surface. The relatively bright regions in [Figs. 7\(e\) and \(f\)](#) show a high concentration of Si and O, which are identical with the precipitated layer in [Fig. 7\(b\)](#). This fact further confirms the SiO₂ layer gradually forms on the ribbon surface. According to results in [Fig. 7](#) and the previous work (such as Ref. [\[16,18\]](#)), the surface behaviors of Fe₇₈Si₉B₁₃ ribbons when applied as peroxides activator might be proposed as follows. (1) Fe on the ribbon surface is consumed by peroxides through corrosion along with the reaction time and the UV–vis irradiation accelerates the surface corrosive behavior; (2) the buried Fe is gradually covered by SiO₂ layer providing protection from further Fe leaching; (3) SiO₂ is easier to be shaken off during mechanical stirring so that Fe₇₈Si₉B₁₃ ribbons can react with peroxides if necessary, which results in the high reusability of Fe₇₈Si₉B₁₃ ribbons.

4. Conclusion

In this work, the generation rates of dominant radical ($\cdot\text{OH}$ or $\text{SO}_4^{\cdot-}$) for three common peroxides (H_2O_2 , PS and PMS) activated by $\text{Fe}_{78}\text{Si}_9\text{B}_{13}$ glassy ribbons under UV–vis irradiation are measured. The order of a dominant radical generation rate at this work is PS > H_2O_2 > PMS. In addition, the $\text{Fe}_{78}\text{Si}_9\text{B}_{13}$ glassy ribbon shows a superior activation ability for H_2O_2 , PS and PMS compared with other Fe-based materials. This fact is further confirmed by the oxidative degradation of CV dye. All the dye solutions can be completely degraded by separately using H_2O_2 , PS and PMS activated by $\text{Fe}_{78}\text{Si}_9\text{B}_{13}$ ribbons under UV–vis irradiation, where only less than 15 min is needed for all peroxides. The quenching tests for the dye oxidative degradation confirm the generation of dominant radical in H_2O_2 ($\cdot\text{OH}$), PS ($\text{SO}_4^{\cdot-}$) and PMS ($\text{SO}_4^{\cdot-}$). The mechanisms of peroxides radical generation and the activation behavior of $\text{Fe}_{78}\text{Si}_9\text{B}_{13}$ glassy ribbon are discussed. The PMS activation by $\text{Fe}_{78}\text{Si}_9\text{B}_{13}$ metallic glass under UV–vis irradiation is also demonstrated, which has not yet been reported. The difference of ribbon surface morphology after 5th run reused indicates that the inclusion of Si leading to formation of SiO_2 layer plays an important role in the surface stability of ribbons. The measurement of radical generation rate provides a novel method to evaluate the activation ability of different materials. The $\text{Fe}_{78}\text{Si}_9\text{B}_{13}$ metallic glass used in this work demonstrates the high activation efficiency and strong surface stability, which shows a potential application of cost-effectiveness improvement in the wastewater treatment.

Acknowledgements

Financial supports from the ECU Innovator Awards [Project No. 23641], Australian Research Council Discovery Project [DP130103592] and National Science Foundation of China (Grant Nos. 61671206, 51771103) are gratefully acknowledged.

References

- [1] Y. Liu, J. Padmanabhan, B. Cheung, J. Liu, Z. Chen, B.E. Scanley, D. Wesolowski, M. Pressley, C.C. Broadbridge, S. Altman, U.D. Schwarz, T.R. Kyriakides, J. Schroers, *Sci. Rep.* 6 (2016) 26950.
- [2] J. Schroers, *JOM* 57 (2005) 35–39.
- [3] D.S. Song, J.H. Kim, E. Fleury, W.T. Kim, D.H. Kim, *J. Alloys Compd.* 389 (2005) 159–164.
- [4] M. Calin, L.C. Zhang, J. Eckert, *Scr. Mater.* 57 (2007) 1101–1104.
- [5] J.Q. Wang, J.Y. Qin, X.N. Gu, Y.F. Zheng, H.Y. Bai, *J. Non-Cryst. Solids* 357 (2011) 1232–1234.
- [6] J.Q. Wang, Y.H. Liu, M.W. Chen, D.V. Louguine-Luzgin, A. Inoue, J.H. Perepezko, *Sci. Rep.* 2 (2012) 418.
- [7] P. Wang, J.Q. Wang, H. Li, H. Yang, J. Huo, J. Wang, C. Chang, X. Wang, R.W. Li, G. Wang, *J. Alloys Compd.* 701 (2017) 759–767.
- [8] X.D. Qin, Z.W. Zhu, G. Liu, H.M. Fu, H.W. Zhang, A.M. Wang, H. Li, H.F. Zhang, *Sci. Rep.* 5 (2015) 18226.
- [9] C. Zhang, H. Zhang, M. Lv, Z. Hu, *J. Non-Cryst. Solids* 356 (2010) 1703–1706.
- [10] J.Q. Wang, Y.H. Liu, M.W. Chen, G.Q. Xie, D.V. Louguine-Luzgin, A. Inoue, J.H. Perepezko, *Adv. Funct. Mater.* 22 (2012) 2567–2570.
- [11] S. Xie, P. Huang, J.J. Krizic, X. Zeng, H. Qian, *Sci. Rep.* 6 (2016) 21947.
- [12] P.P. Wang, J.Q. Wang, J.T. Huo, W. Xu, X.M. Wang, G. Wang, *Sci. China Phys. Mech. Astron.* 60 (2017) 076112.
- [13] S.Q. Chen, G.N. Yang, S.T. Luo, S.J. Yin, J.L. Jia, Z. Li, S.H. Gao, Y. Shao, K.F. Yao, *J. Mater. Chem. A* 5 (2017) 14230–14240.
- [14] S.Q. Chen, N. Chen, M.T. Cheng, S.T. Luo, Y. Shao, K.F. Yao, *Intermetallics* 90 (2017) 30–35.
- [15] Z. Jia, X. Duan, P. Qin, W. Zhang, W. Wang, C. Yang, H. Sun, S. Wang, L.C. Zhang, *Adv. Funct. Mater.* (2017), <http://dx.doi.org/10.1002/adfm.201702258>.
- [16] Z. Jia, X. Duan, W. Zhang, W. Wang, H. Sun, S. Wang, L.C. Zhang, *Sci. Rep.* 6 (2016) 38520.
- [17] S.X. Liang, Z. Jia, W.C. Zhang, W.M. Wang, L.C. Zhang, *Mater. Des.* 119 (2017) 244–253.
- [18] Z. Jia, J. Kang, W.C. Zhang, W.M. Wang, C. Yang, H. Sun, D. Habibi, L.C. Zhang, *Appl. Catal. B Environ.* 204 (2017) 537–547.
- [19] Z. Jia, S.X. Liang, W.C. Zhang, W.M. Wang, C. Yang, L.C. Zhang, *J. Taiwan Inst. Chem. Eng.* 71 (2017) 128–136.
- [20] Z. Jia, W.C. Zhang, W.M. Wang, D. Habibi, L.C. Zhang, *Appl. Catal. B Environ.* 192 (2016) 46–56.
- [21] W. Chu, C.W. Ma, *Water Res.* 34 (2000) 3153–3160.
- [22] Z. Jia, L.B.T. La, W.C. Zhang, S.X. Liang, B. Jiang, S.K. Xie, D. Habibi, L.C. Zhang, *J. Mater. Sci. Technol.* 33 (2017) 856–863.
- [23] Z. Jia, J. Miao, H.B. Lu, D. Habibi, W.C. Zhang, L.C. Zhang, *J. Taiwan Inst. Chem. Eng.* 60 (2016) 267–274.
- [24] J. Miao, Z. Jia, H.B. Lu, D. Habibi, L.C. Zhang, *J. Taiwan Inst. Chem. Eng.* 45 (2014) 1636–1641.
- [25] S.Y. Oh, H.W. Kim, J.M. Park, H.S. Park, C. Yoon, *J. Hazard. Mater.* 168 (2009) 346–351.
- [26] A. Rastogi, S.R. Al-Abed, D.D. Dionysiou, *Appl. Catal. B Environ.* 85 (2009) 171–179.
- [27] X.F. Li, S.X. Liang, X.W. Xi, Z. Jia, S.K. Xie, H.C. Lin, J.P. Hu, L.C. Zhang, *Metals* 7 (2017) 273.
- [28] M.E. Lindsey, M.A. Tarr, *Chemosphere* 41 (2000) 409–417.
- [29] P. Neta, R.E. Huie, A.B. Ross, *J. Phys. Chem. Ref. Data* 17 (1988) 1027–1284.
- [30] S. Yang, P. Wang, X. Yang, L. Shan, W. Zhang, X. Shao, R. Niu, *J. Hazard. Mater.* 179 (2010) 552–558.
- [31] H. Li, J. Wan, Y. Ma, Y. Wang, M. Huang, *J. Chem. Eng.* 237 (2014) 487–496.
- [32] M.I. Pariente, F. Martínez, J.A. Melero, J.Á. Botas, T. Velegakis, N.P. Xekoukoulotakis, D. Mantzavinos, *Appl. Catal. B Environ.* 85 (2008) 24–32.
- [33] Z. Zhang, M.F. Hossain, T. Takahashi, *Appl. Catal. B Environ.* 95 (2010) 423–429.
- [34] Q. Lan, F. Li, C. Liu, X.Z. Li, *Environ. Sci. Technol.* 42 (2008) 7918–7923.
- [35] J. Bandara, J.A. Mielczarski, A. Lopez, J. Kiwi, *Appl. Catal. B Environ.* 34 (2001) 321–333.
- [36] Y. Nie, C. Hu, L. Zhou, J. Qu, *Appl. Catal. B Environ.* 82 (2008) 151–156.
- [37] L. Guo, F. Chen, X. Fan, W. Cai, J. Zhang, *Appl. Catal. B Environ.* 96 (2010) 162–168.
- [38] L.C.A. Oliveira, M. Gonçalves, M.C. Guerreiro, T.C. Ramalho, J.D. Fabris, M.C. Pereira, K. Sapag, *Appl. Catal. A Gen.* 316 (2007) 117–124.
- [39] I.R. Guimaraes, A. Giroto, L.C.A. Oliveira, M.C. Guerreiro, D.Q. Lima, J.D. Fabris, *Appl. Catal. B Environ.* 91 (2009) 581–586.
- [40] G.D. Fang, D.D. Dionysiou, S.R. Al-Abed, D.M. Zhou, *Appl. Catal. B Environ.* 129 (2013) 325–332.
- [41] Y. Liu, H. Guo, Y. Zhang, W. Tang, *RSC Adv.* 6 (2016) 79910–79919.
- [42] Q. Yang, H. Choi, S.R. Al-Abed, D.D. Dionysiou, *Appl. Catal. B Environ.* 88 (2009) 462–469.
- [43] X. Wang, Y. Pan, Z. Zhu, J. Wu, *Chemosphere* 117 (2014) 638–643.
- [44] L.C. Zhang, J. Xu, *J. Non-Cryst. Solids* 347 (2004) 166–172.
- [45] H.B. Lu, L.C. Zhang, A. Gebert, L. Schultz, *J. Alloys Compd.* 462 (2008) 60–67.
- [46] C. Liang, C.F. Huang, N. Mohanty, R.M. Kurakalva, *Chemosphere* 73 (2008) 1540–1543.
- [47] Q. Zhang, S. Fu, H. Li, Y. Liu, *BioResources* 8 (2013) 3699–3705.
- [48] X.J. Yang, X.M. Xu, J. Xu, Y.F. Han, *J. Am. Chem. Soc.* 135 (2013) 16058–16061.
- [49] W.P. Kwan, B.M. Voelker, *Environ. Sci. Technol.* 37 (2003) 1150–1158.
- [50] P. Neta, V. Madhavan, H. Zemel, R.W. Fessenden, *J. Am. Chem. Soc.* 99 (1977) 163–164.
- [51] W.D. Oh, Z. Dong, T.T. Lim, *Appl. Catal. B Environ.* 194 (2016) 169–201.
- [52] F. Ji, C. Li, L. Deng, *Chem. Eng. J.* 178 (2011) 239–243.
- [53] L.C. Zhang, J. Xu, E. Ma, *J. Mater. Res.* 17 (2002) 1743–1749.
- [54] L.C. Zhang, Z.Q. Shen, J. Xu, *J. Mater. Res.* 18 (2003) 2141–2149.
- [55] L.C. Zhang, J. Xu, J. Eckert, *J. Appl. Phys.* 100 (2006) 033514.
- [56] Z.H. Lai, Y.S. Chao, H. Conrad, K. Chu, *J. Mater. Res.* 10 (1995) 900–906.
- [57] A. Wang, C. Zhao, H. Men, A. He, C. Chang, X. Wang, R.W. Li, *J. Alloys Compd.* 630 (2015) 209–213.
- [58] J. Yang, X. Bian, Y. Bai, X. Lv, P. Wang, *J. Non-Cryst. Solids* 358 (2012) 2571–2574.
- [59] C. Liang, H.W. Su, *Ind. Eng. Chem. Res.* 48 (2009) 5558–5562.
- [60] Y. Yang, J. Jiang, X. Lu, J. Ma, Y. Liu, *Environ. Sci. Technol.* 49 (2015) 7330–7339.
- [61] X. Hou, X. Huang, Z. Ai, J. Zhao, L. Zhang, *J. Hazard. Mater.* 310 (2016) 170–178.
- [62] C. Luo, J. Ma, J. Jiang, Y. Liu, Y. Song, Y. Yang, Y. Guan, D. Wu, *Water Res.* 80 (2015) 99–108.
- [63] J. Wu, H. Gao, S. Yao, L. Chen, Y. Gao, H. Zhang, *Sep. Purif. Technol.* 147 (2015) 179–185.
- [64] H.J. Fan, S.T. Huang, W.H. Chung, J.L. Jan, W.Y. Lin, C.C. Chen, *J. Hazard. Mater.* 171 (2009) 1032–1044.
- [65] C.C. Chen, W.C. Chen, M.R. Chiou, S.W. Chen, Y.Y. Chen, H.J. Fan, *J. Hazard. Mater.* 196 (2011) 420–425.
- [66] X. Duan, H. Sun, J. Kang, Y. Wang, S. Indrawirawan, S. Wang, *ACS Catal.* 5 (2015) 4629–4636.
- [67] H. Sun, G. Zhou, S. Liu, H.M. Ang, M.O. Tadé, S. Wang, *ACS Appl. Mater. Interfaces* 4 (2012) 6235–6241.